Available online at www.sciencedirect.com
SCIENCE DIRECT®
International Journal of Solids and Structures 42 (2005) 2559–2573
INTERNATIONAL JOURNAL OF SOLIDS and STRUCTURES
www.elsevier.com/locate/ijsolstr

Instabilities in power law gradient hardening materials

Christian F. Niordson *, Viggo Tvergaard

Department of Mechanical Engineering, Solid Mechanics, Technical University of Denmark, Nils Koppels Alle, Building 404, DK-2800 Kgs. Lyngby, Denmark

Received 6 July 2004; received in revised form 30 September 2004
Available online 30 November 2004

Abstract

Tension and compression instabilities are investigated for specimens with dimensions in the micron range. A finite strain generalization of a higher order strain gradient plasticity theory is implemented in a finite element scheme capable of modeling power law hardening materials. Effects of gradient hardening are found to delay the onset of localization under plane strain tension, and significantly reduce strain gradients in the localized zone. For plane strain compression gradient hardening is found to increase the load-carrying capacity significantly.

Keywords: Localization; Buckling; Strain gradient plasticity; Size effects; Finite strain; Elastic–plastic material; Finite elements

1. Introduction

For thin metal plates or free standing thin films that play an important role in applications ranging from microelectro-mechanical systems to coatings the mechanical properties are not well described by conventional plasticity theory. The material models must account for observed size-effects (Fleck et al., 1994; Ma and Clarke, 1995; Fleck and Hutchinson, 1997; Stölken and Evans, 1998; Begley and Hutchinson, 1998; Haque and Saif, 2003), and a variety of such material models have been developed by incorporating gradient effects in the constitutive and equilibrium equations.

Instabilities under tensile or compressive loading are important limitations of the load-carrying capacity for thin plates or films. For the plane strain tension test (Hill and Hutchinson, 1975), or the plane strain compression test (Young, 1976), the critical stresses for bifurcation into diffuse modes have been determined, dependent on the ratio of the wave-length to the plate thickness, and the regimes have been

* Corresponding author. Tel.: +45 4525 4287; fax: +45 4593 1475.
E-mail address: cn@mek.dtu.dk (C.F. Niordson).

0020-7683/$ - see front matter
doi:10.1016/j.ijsolstr.2004.09.051

identified, where the governing equations are elliptic, parabolic or hyperbolic. Size-effects have been incorporated into these bifurcation analyses by Benallal and Tvergaard (1995), who used a finite strain version of the gradient plasticity model proposed by Mühlhaus and Aifantis (1991). In addition to the two material moduli μ and μ^* appearing in the previous bifurcation analyses, this gradient theory of plasticity also incorporates a characteristic material length scale l. It has been found that for very small values of the material length the value of the lowest bifurcation stress is practically unaffected by nonlocal effects, but when the wave-length decays towards the material length, the bifurcation is more and more delayed by the nonlocal effects.

The nonlocal plasticity model used in the present paper is a finite strain generalization recently developed by Niordson and Redanz (2004) for the strain gradient plasticity theory by Fleck and Hutchinson (2001). For plane strain specimens in tension or compression the focus here is on determining how much the onset of instability is delayed, or the load-carrying capacity increased, when the specimen size is as small as the characteristic material length, or even smaller. In these analyses the presence of initial geometrical imperfections is accounted for. The bifurcation analyses mentioned above have shown that both for tension and compression instabilities occur in symmetric modes as well as anti-symmetric modes. However, for longer wave-lengths symmetric modes give the lowest bifurcation stress in tension, leading to necking, and anti-symmetric modes give the first bifurcation in compression, leading to column buckling. Therefore, these will be the only cases considered in the present studies.

Necking in plane strain tension was also analyzed by Niordson and Redanz (2004) for a linear hardening solid. Their numerical implementation of the gradient plasticity theory did not give good convergence for power law hardening materials. This is resolved here by using higher order elements in the numerical implementation, and the results shown are for power law hardening.

2. Material model

The material behavior is modeled by a finite strain generalization proposed by Niordson and Redanz (2004) for the strain gradient plasticity theory by Fleck and Hutchinson (2001). An updated Lagrangian formulation is used to model the strain gradient effects at finite strains based on the work of McMeeking and Rice (1975) and Yamada and Sasaki (1995).

In the strain gradient plasticity theory by Fleck and Hutchinson (2001) gradient hardening is introduced through the gradient of the plastic strain rate

$$\rho_{ijk} = \rho_{jik} = \dot{\epsilon}^{\mathrm{P}}_{ij,k} \tag{1}$$

Plastic work in the material is due to an effective plastic strain, E^{P}, defined in terms of the conventional definition of effective plastic strain, $\dot{\epsilon}^{\mathrm{P}^2} = \frac{2}{3}\dot{\epsilon}^{\mathrm{P}}_{ij}\dot{\epsilon}^{\mathrm{P}}_{ij}$, and three invariants of homogeneous degree two of the gradient of the plastic strain rate, ρ_{ijk}. Denoting these invariants by I_1, I_2 and I_3, the effective plastic strain is defined by the incremental relation

$$\dot{E}^{\mathrm{P}^2} = \dot{\epsilon}^{\mathrm{P}^2} + l_1^2 I_1 + 4 l_2^2 I_2 + \frac{8}{3} l_3^2 I_3 \tag{2}$$

where l_1, l_2 and l_3 are material length parameters introduced for dimensional consistency, and the numerical coefficients of the invariants are chosen such that the material length parameters in the theory have similar meaning as the length parameters in the strain gradient theory of Fleck and Hutchinson (1997) (see Fleck and Hutchinson, 2001).

The plastic strain increment is defined according to the usual relation for J_2 flow theory

$$\dot{\epsilon}^{\mathrm{P}}_{ij} = \frac{3}{2}\frac{S_{ij}}{\sigma_{(e)}}\dot{\epsilon}^{\mathrm{P}} \tag{3}$$

where S_{ij} is the deviator of the Cauchy stress σ_{ij}, and $\sigma_{(e)} = \sqrt{\frac{3}{2}S_{ij}S_{ij}}$ is von Mises' effective stress.

Expressing the plastic strain rate as the product of its magnitude, $\dot{\epsilon}^{\mathrm{P}} = \sqrt{\frac{2}{3}\dot{\epsilon}^{\mathrm{P}}_{ij}\dot{\epsilon}^{\mathrm{P}}_{ij}}$, and its direction, $m_{ij} = \frac{3}{2}S_{ij}/\sigma_{(e)}$, gives the following expression for ρ_{ijk}

$$\rho_{ijk} = (m_{ij}\dot{\epsilon}^{\mathrm{P}})_{,k} = m_{ij,k}\dot{\epsilon}^{\mathrm{P}} + m_{ij}\dot{\epsilon}^{\mathrm{P}}_{,k} \tag{4}$$

which shows how ρ_{ijk} depends on the conventional effective plastic strain and its gradient, as well as on the direction of the plastic strain increment and its gradient, $m_{ij,k}$. Introducing this relation in the expression for the effective plastic strain (Eq. (2)) gives

$$\dot{E}^{\mathrm{P}^2} = \dot{\epsilon}^{\mathrm{P}^2} + A_{ij}\dot{\epsilon}^{\mathrm{P}}_{,i}\dot{\epsilon}^{\mathrm{P}}_{,j} + B_i\dot{\epsilon}^{\mathrm{P}}_{,i}\dot{\epsilon}^{\mathrm{P}} + C\dot{\epsilon}^{\mathrm{P}^2} \tag{5}$$

where the tensors A_{ij}, B_i and C depend on the three material length parameters l_1, l_2, and l_3 as well as on the spatial gradients of the plastic strain increment direction (for details see Fleck and Hutchinson, 2001).

Within the framework of the present theory, a single parameter theory closely related to the strain gradient theory of Aifantis (1984) can be formulated. This is done by defining the measure of the effective plastic strain as

$$\dot{E}^{\mathrm{P}^2} = \dot{\epsilon}^{\mathrm{P}^2} + l_*^2\dot{\epsilon}^{\mathrm{P}}_{,i}\dot{\epsilon}^{\mathrm{P}}_{,i} \tag{6}$$

where l_* is a new material length parameter (Fleck and Hutchinson, 2001). This single parameter version is not a special case of the general theory based on Eq. (2), even though it does fit within the same theoretical framework.

The principle of virtual work for the strain gradient plasticity theory used is expressed in the current configuration by

$$\int_V (\sigma_{ij}\delta\dot{\epsilon}_{ij} + (Q - \sigma_{(e)})\delta\dot{\epsilon}^{\mathrm{P}} + \tau_i\delta\dot{\epsilon}^{\mathrm{P}}_{,i})\,\mathrm{d}V = \int_S (T_i\delta\dot{u}_i + t\delta\dot{\epsilon}^{\mathrm{P}})\,\mathrm{d}S \tag{7}$$

where ϵ_{ij} is the total strain, Q is the work conjugate to the plastic strain, and τ_i is the higher order stress which is work conjugate to the gradient of ϵ^{P}. The volume and the surface of the solid are denoted V and S, respectively, and the outward unit normal is denoted N_i. Due to the higher order nature of Eq. (7) boundary conditions have to be applied for the higher order traction $t = \tau_i N_i$ or for the plastic strain ϵ^{P}, in addition to the conditions on the tractions $T_i = \sigma_{ij}N_j$ or the displacements u_i. The higher order boundary conditions must be applied to the exterior of the plastically deforming parts of the solid, which in general includes internal elastic–plastic boundaries.

With J denoting the determinant of the metric tensor in the deformed geometry the Kirchhoff type stresses are defined by

$$\varsigma_{ij} = J\sigma_{ij} \tag{8}$$

$$\sigma^{\varsigma}_{(e)} = J\sigma_{(e)} \tag{9}$$

$$\rho_i = J\tau_i \tag{10}$$

$$q = JQ \tag{11}$$

Using the current state as reference we have $J = 1$ (updated Lagrangian formulation), and the principle of virtual work (Eq. (7)) can be expressed in incremental form as follows:

$$\int_V \left(\overset{\nabla}{\varsigma}_{ij} \delta\dot{\epsilon}_{ij} - \sigma_{ij}(2\dot{\epsilon}_{ik}\delta\dot{\epsilon}_{kj} - \dot{e}_{kj}\delta\dot{e}_{ki}) + (\dot{q} - \dot{\sigma}^{\varsigma}_{(e)})\delta\dot{\epsilon}^{\mathrm{P}} + \overset{\vee}{\rho}_i \delta\dot{\epsilon}^{\mathrm{P}}_{0,i} \right) \mathrm{d}V = \int_S (\dot{T}_{0i}\delta\dot{u}_i + \dot{t}_0 \delta\dot{\epsilon}^{\mathrm{P}})\,\mathrm{d}S \tag{12}$$

Here, the spatial derivative of the effective plastic strain $\dot{\epsilon}^{\mathrm{P}}_{0,i}$ is evaluated in the reference coordinate system, and $\dot{T}_{0i}$ and $\dot{t}_0$ are the nominal traction rates. This relation is identical to the expressions derived in McMeeking and Rice (1975) and Yamada and Sasaki (1995) when excluding higher order terms. The symbol $\overset{\nabla}{(\ )}$ denotes the Jaumann rate and $\overset{\vee}{(\ )}$ denotes the convected rate.

The finite strain generalization of the constitutive equations for the stress-measures work-conjugate to the total strain, the plastic strain, and the plastic strain gradient, respectively, are

$$\overset{\nabla}{\varsigma}_{ij} = \mathscr{R}_{ijkl}(\dot{\epsilon}_{kl} - \dot{\epsilon}^{\mathrm{P}} m_{kl}) = \dot{\varsigma}_{ij} - \dot{\omega}_{ik}\sigma_{kj} - \sigma_{ik}\dot{\omega}_{jk} \tag{13}$$

$$\dot{q} - \dot{\sigma}^{\varsigma}_{(e)} = h\left(\dot{\epsilon}^{\mathrm{P}} + \frac{1}{2} B_i \dot{\epsilon}^{\mathrm{P}}_{,i} + C\dot{\epsilon}^{\mathrm{P}} \right) - m_{ij}\overset{\nabla}{\varsigma}_{ij} \tag{14}$$

$$\overset{\vee}{\rho}_i = h\left(A_{ij}\dot{\epsilon}^{\mathrm{P}}_{,j} + \frac{1}{2} B_i \dot{\epsilon}^{\mathrm{P}} \right) = \dot{\rho}_i - \dot{e}_{ik}\rho_k \tag{15}$$

where $\dot{e}_{ij} = \dot{u}_{i,j}$, $\dot{\omega}_{ij}$ is the anti-symmetric part of $\dot{e}_{ij}$ and

$$\mathscr{R}_{ijkl} = \frac{E}{1+\nu}\left(\frac{1}{2}(\delta_{ik}\delta_{jl} + \delta_{il}\delta_{jk}) + \frac{\nu}{1-2\nu}\delta_{ij}\delta_{kl} \right) \tag{16}$$

The hardening modulus is given by

$$h[E^{\mathrm{P}}] = \left(\frac{1}{E_{\mathrm{T}}[E^{\mathrm{P}}]} - \frac{1}{E} \right)^{-1} \tag{17}$$

where, E_{T} is the tangent modulus and E is Young's modulus. It is noted that the hardening modulus is evaluated at E^{P} rather than at ϵ^{P} as it would be in a conventional theory.

For the power-law hardening material we use the following expression for the tangent modulus

$$E_{\mathrm{T}} = \frac{E}{n}\left(\frac{E^{\mathrm{P}}}{\epsilon_0} + 1 \right)^{(1/n)-1} \tag{18}$$

which deviates very little from that corresponding to a standard power-law. In this expression $\epsilon_0 = \sigma_y/E$ is the uni-axial yield strain, with σ_y denoting the initial yield stress.

The constitutive equation for the generalized effective stress in (14) can also be expressed by

$$\dot{q} = h\left(\dot{\epsilon}^{\mathrm{P}} + \frac{1}{2} B_i \dot{\epsilon}^{\mathrm{P}}_{,i} + C\dot{\epsilon}^{\mathrm{P}} \right) \tag{19}$$

since $\dot{\sigma}^{\varsigma}_{(e)} = m_{ij}\overset{\nabla}{\varsigma}_{ij}$. Further details on the present strain gradient plasticity theory can be found in Fleck and Hutchinson (2001) and Niordson and Redanz (2004).

3. Numerical method

The numerical solutions are obtained using a finite element method where nodal effective plastic strain increments, $\dot{\epsilon}^{\mathrm{P}}_n$, appear directly as unknowns on equal footing with the nodal displacement increments, $\dot{D}^n$. The structure of the finite element method as it is used in the present study has been used by Vardoulakis

and Aifantis (1991); de Borst and Mühlhaus (1992), and de Borst and Pamin (1996), to model the gradient theory by Aifantis (1984). Niordson and Hutchinson (2003) have used it to model the small strain theory by Fleck and Hutchinson (2001), and Niordson and Redanz (2004) have used it to model finite strain effects in plane strain sheet necking for linearly hardening materials.

The displacement increments, $\dot{u}_i$, and the effective plastic strain increments, $\dot{\epsilon}^{\mathrm{P}}$, are interpolated within each element between the nodal displacement increments, $\dot{D}^n$, and the nodal effective plastic strain increments, $\dot{\epsilon}^{\mathrm{P}}_n$, respectively

$$\dot{u}_i = \sum_{n=1}^{2k} N_i^n \dot{D}^n \qquad \dot{\epsilon}^{\mathrm{P}} = \sum_{n=1}^{l} M^n \dot{\epsilon}^{\mathrm{P}}_n \tag{20}$$

Here, N_i^n and M^n are shape functions, and k and l are the number of nodes used for the displacement interpolation and the effective plastic strain interpolation, respectively.

Triangular elements with $k = l = 3$ were used by Niordson and Redanz (2004). Here, it has been found that much better convergence is obtained for power law hardening materials, when eight node serendipity elements are used for interpolating both the displacements and the effective plastic strain, so that $k = l = 8$ in the above equations. These iso-parametric elements with quadratic shape functions use only boundary nodes (Zienkiewicz, 1977). The appropriate derivatives of the displacement field and the effective plastic strain field can be expressed as

$$\dot{e}_{ij} = \sum_{n=1}^{2k} N_{i,j}^n \dot{D}^n \quad \dot{\epsilon}_{ij} = \sum_{n=1}^{2k} E_{ij}^n \dot{D}^n \quad \dot{\epsilon}^{\mathrm{P}}_{,i} = \sum_{n=1}^{l} M^n_{,i} \dot{\epsilon}^{\mathrm{P}}_n \tag{21}$$

with

$$E_{ij}^n = \frac{1}{2}(N_{i,j}^n + N_{j,i}^n) \tag{22}$$

Using these relations in the principle of virtual work (Eq. (12)), which must hold for arbitrary variations of $\delta\dot{D}^n$ and $\delta\dot{\epsilon}^{\mathrm{P}}_n$, the discretized equations can now be written in the following form

$$\begin{bmatrix} \boldsymbol{K_e} & \boldsymbol{K_{ep}} \\ \boldsymbol{K_{ep}^T} & \boldsymbol{K_p} \end{bmatrix} \begin{bmatrix} \dot{\boldsymbol{D}} \\ \dot{\boldsymbol{\epsilon}}^{\mathrm{P}} \end{bmatrix} = \begin{bmatrix} \dot{\boldsymbol{F}}_{\boldsymbol{1}} \\ \dot{\boldsymbol{F}}_{\boldsymbol{2}} \end{bmatrix} \tag{23}$$

where

$$\boldsymbol{K_e^{nm}} = \int_V (E_{ij}^n \mathscr{R}_{ijkl} E_{kl}^m + \sigma_{ij}(N_{k,j}^m N_{k,i}^n - 2E_{ik}^m E_{kj}^n))\,\mathrm{d}V \tag{24}$$

is the elastic stiffness matrix,

$$\boldsymbol{K_{ep}^{nm}} = -\int_V (E_{ij}^n \mathscr{R}_{ijkl} m_{kl} M^m)\,\mathrm{d}V \tag{25}$$

is a matrix of dimension force, and

$$\boldsymbol{K_p^{nm}} = \int_V \left(m_{ij}\mathscr{R}_{ijkl} m_{kl} M^m M^n + h\left(M^m M^n + A_{ij} M^m_{,j} M^n_{,i} + \frac{1}{2} B_i (M^m_{,i} M^n + M^m M^n_{,i}) + C M^m M^n \right) \right) \mathrm{d}V \tag{26}$$

is a matrix of dimension energy.

The right-hand side of Eq. (23) consists of two components,

$$\dot{\boldsymbol{F}}_{\boldsymbol{1}}^n = \int_S \dot{T}_{0i} N_i^n \,\mathrm{d}S \quad \text{and} \quad \dot{\boldsymbol{F}}_{\boldsymbol{2}}^n = \int_S \dot{t}_0 M^n \,\mathrm{d}S \tag{27}$$

When the nodal displacement increments and effective plastic strain increments have been determined, the elastic strains are calculated, and then the Jaumann rate of the stress and the convected rate of the higher order stress can be found according to Eqs. (13) and (15). The increments of the stress tensor and the higher order stress vector are then calculated by

$$\dot{\sigma}_{ij} = \overset{\nabla}{\varsigma}_{ij} + \dot{\omega}_{ik}\sigma_{kj} + \sigma_{ik}\dot{\omega}_{jk} - \sigma_{ij}\dot{\epsilon}_{kk} \tag{28}$$

$$\dot{\tau}_i = \overset{\vee}{\rho}_i + \dot{e}_{ik}\tau_k - \tau_i\dot{\epsilon}_{kk} \tag{29}$$

Plastic yielding is initiated when $\sigma_{(e)}$ becomes larger than the initial yield stress, σ_y. Elastic unloading at an integration point starts, when the solution has found a negative increment of the effective plastic strain at that integration point in the previous increment. Plastic yielding starts again when Q reaches Q_y, which is updated using Eq. (19) and the incremental form of Eq. (11). The present strain gradient plasticity theory reduces to J_2 finite strain theory when all material length parameters are set to zero.

Boundary conditions on internal elastic–plastic boundaries are either applied as vanishing higher order traction rate, $\dot{t} = 0$, or conversely vanishing plastic strain rate, $\dot{\epsilon}^{\mathrm{P}} = 0$. For these two boundary conditions the work on the internal boundaries vanish, which would not be the case if intermediate boundary conditions were considered. When imposing a vanishing higher order traction rate on internal boundaries $\boldsymbol{K_p}$ is multiplied by 10^{-4} for Gauss points in the elastic region. When imposing a vanishing plastic strain rate on internal boundaries $\boldsymbol{K_p}$ is multiplied by 10^{8} for Gauss points in the elastic region.

In all cases studied it has been checked that a sufficiently refined mesh has been used. It is noted that the use of gradients here is motivated by physical properties of the material studied, and is not considered a numerical tool to avoid discretization sensitivity. The typical meshes employ eight elements through the half width of the specimen. The number of elements along the length of the specimens depend on the aspect ratio. For some of the shorter specimens in the necking studies 16 and even 32 elements through half the width have been used, so that a sufficient number of elements along the length could be used keeping the aspect ratio of the elements reasonable. Along the length of the specimen, stretching of the mesh has been used for the necking studies to ensure that the aspect ratio of the elements in the neck is reasonable throughout the analyses.

4. Results

The plane strain tension test and the plane strain compression test are here analyzed for specimens with dimensions in the micron range. Fig. 1a shows the geometry for the plane strain tension test. The specimen has the width $2a_0$ and the length $2b_0$, and an initial symmetric cosine imperfection of initial amplitude δ_0. Along the horizontal edges displacements are prescribed to enforce tension in the vertical direction, while shear stresses vanish. The vertical edges are stress free. After some elongation the deformation begins to localize, and the onset of localization is defined as the point when elastic unloading initiates somewhere in the specimen.

Fig. 1b shows the geometry for the plane strain compression test. An initial anti-symmetric cosine imperfection is used so that anti-symmetric buckling modes are triggered. Along the horizontal edges displacements are prescribed to enforce compression in the vertical direction, while shear stresses vanish. The vertical edges are stress free. At some level of the overall deformation plastic buckling will occur, when elastic unloading initiates at a material point in the specimen.

For both the tension and the compression problem the maximum width and the length of the deformed specimens are denoted $2a$ and $2b$, respectively. The amplitude of the neck and the buckling mode amplitude are denoted by δ.

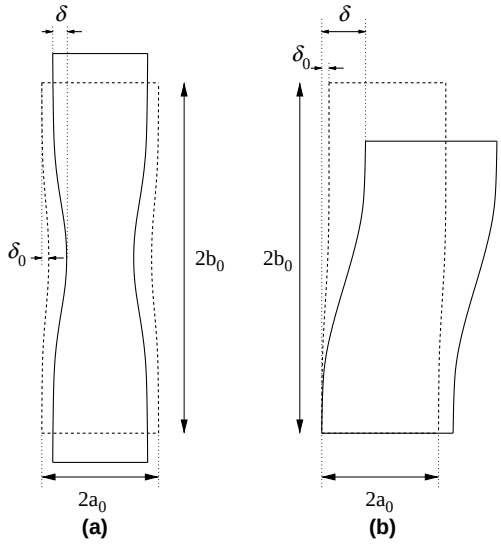

Fig. 1. The geometry of the specimen in the undeformed configuration (dashed line) and in the deformed state (solid line). The amplitude of the imperfection is denoted δ, and it has the value δ_0 in the undeformed configuration. (a) shows the geometry for the tension analyses, and (b) for the compression analyses.

The higher order boundary condition on the outer surface of the specimen is $t = 0$. On internal elastic–plastic boundaries the higher order traction rate is here taken to vanish ($\dot{t} = 0$). Whether this internal boundary condition or the alternative boundary condition of a full constraint on the increment of the plastic flow ($\dot{\epsilon}^{\mathrm{P}} = 0$) is used, has been found to have a negligible effect on the problems studied within the present paper.

4.1. Tension

Results for a rather short and stubby plane strain tensile test specimen, with $b_0/a_0 = 3.0$, are shown in Fig. 2. Here, the average nominal tensile stress is denoted σ_n and the average logarithmic strain is denoted ϵ_{av}. The small initial imperfection in the width is specified by $\delta_0/a_0 = 0.005$ and the material parameters are $\sigma_y/E = 0.004$, $\nu = 0.3$, and $n = 10$. The star on the curves indicate the maximum load point, while the circles show the onset of localization (elastic unloading). The curve for conventional theory shows the behavior known from many previous analyses of the plane strain tensile test, i.e., the maximum load occurs at $\epsilon_{av} = 1/n$ and the onset of localization occurs with a little delay after the maximum. Subsequently, as the localized neck develops, the load drops down below the level corresponding to continued uniform deformation. Fig. 2 also shows results for gradient dependent materials. One curve corresponds to the single parameter theory with $l_*/a_0 = 0.5$, and results for the multi-parameter theory are shown with each of the three length parameters set equal to $0.5a_0$, while the other two are zero. For this case the gradient effect gives a significant extra delay of the onset of localization, after the load maximum, and also the subsequent load decay during neck evolution occurs more slowly than found for the conventional theory. It is clear in Fig. 2 that there is rather little difference between the four curves representing gradient effects, when the values of the four different material lengths are the same.

A case rather similar to that in Fig. 2 was analyzed by Niordson and Redanz (2004), with the main difference that they considered a linear hardening material with the tangent modulus $E_{\mathrm{T}} = E/40$. This gave a load maximum at a much larger strain, $\epsilon_{av} \approx 0.7$, and subsequently a decaying load as localized necking

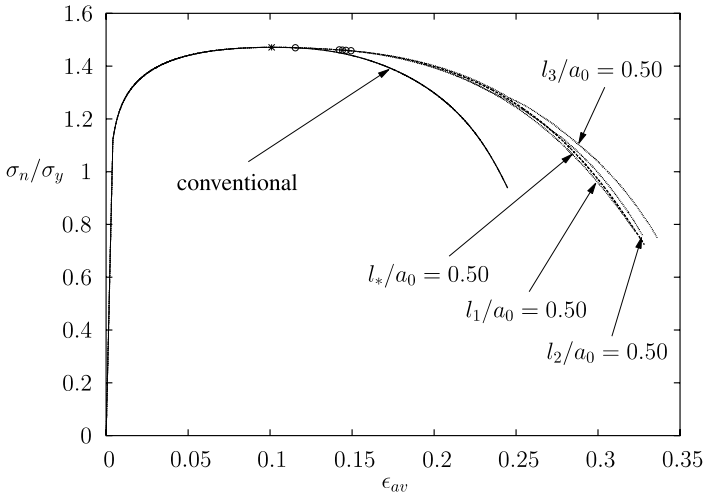

Fig. 2. Overall response in tension for specimens characterized by the geometrical parameters $b_0/a_0 = 3.0$, and $\delta_0/a_0 = 5.0 \times 10^{-3}$, and the material parameters $\sigma_y/E = 0.004$, $\nu = 0.3$, and $n = 10$. The solid curve shows results for a conventional material, while the dashed curve shows results for materials with $l_*/a_0 = 0.50$. The three dotted curves show the results for the multi-parameter theory with each of the material length parameter set equal to $a_0/2$ one by one keeping the others zero.

developed. But apart from the much larger strains the behavior was similar to that shown in Fig. 2 in that the gradient effect gave a significant delay of the onset of localization and there was little difference between the four curves representing gradient effects analogous to those in Fig. 2.

In Fig. 3, for $n = 10$, two of the curves were also shown in Fig. 2, but in addition to the curve for $l_*/a_0 = 0.5$ according to the single parameter gradient theory results are also shown for the values 0.25, 1.0, and 2.0. This comparison shows a very strong sensitivity to the value of the characteristic material length relative to specimen dimensions, particularly in this range where so small specimens are considered

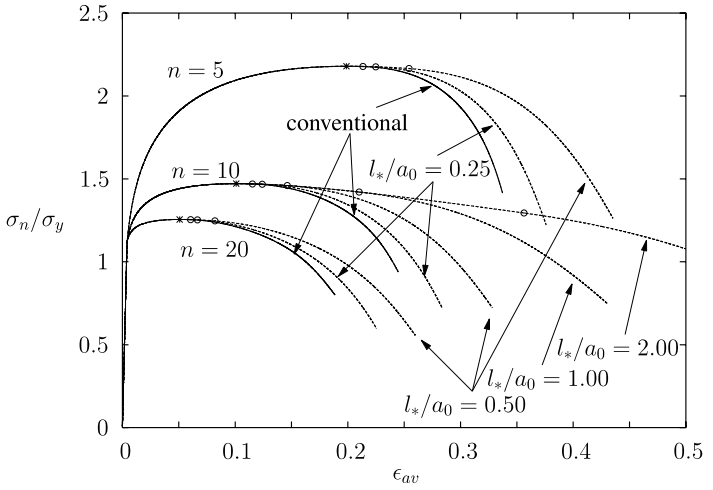

Fig. 3. Overall response in tension for specimens with different hardening exponents. The geometrical parameters are $b_0/a_0 = 3.0$ and $\delta_0/a_0 = 5.0 \times 10^{-3}$, and the material parameters $\sigma_y/E = 0.004$, and $\nu = 0.3$. The solid curves show results for a conventional material, while the dashed curves show results for gradient dependent materials with different material length scales.

that the material length exceeds the specimen size. For increasing values of the material length parameter, the onset of localization is further delayed relative to the maximum load point. For $l_*/a_0 = 2.0$ the onset of localization occurs much after the load maximum, and also the subsequent necking develops slowly. Fig. 3 also shows the effect of the strain hardening exponent by including curves for $n = 5$ and 20. For each of these strain hardening levels the curves behave essentially as described for $n = 10$. As expected, both the load levels and the strains at the maximum and at localization increase much with the level of strain hardening.

With the initial aspect ratio $b_0/a_0 = 3$, analyzed in Figs. 2 and 3 the current aspect ratio at the onset of localization for $n = 10$ is $b/a \approx 3.8$ for the conventional material and even higher for the gradient dependent materials, so that the wave-length of the corresponding bifurcation mode is several times the current specimen width at bifurcation. In Fig. 4, for larger values of the initial aspect ratio b_0/a_0, the wave-length of the bifurcation mode governing the onset of localization is larger than that in Fig. 2, relative to the current width. All these cases are in the range of conventional necking behavior, where the limit of $b_0/a_0 \to \infty$ gives the Considére condition that necking initiates at the load maximum, but where the onset of localization is delayed for a finite aspect ratio, with a larger delay beyond the load maximum the smaller value of b_0/a_0. In all the cases the onset of localization is further delayed by the effect of a material length scale.

Smaller values of the initial aspect ratio b_0/a_0 are considered in Fig. 5, where the smallest value, $b_0/a_0 = 0.125$, starts to look more like a surface wave instability than a necking mode instability. We see that for the two smaller values of b_0/a_0 there is a very significant delay of the onset of localization when gradient effects are present. In the case of $b_0/a_0 = 0.125$ the onset of localization for the conventional material occurs at the current aspect ratio $b/a \approx 0.40$, but for $l_*/a_0 = 0.5$ this current aspect ratio has grown much more, to 3.0, when localization occurs, and at this point $l_*/a \approx 2.5$. The bifurcation analyses of Benallal and Tvergaard (1995) have shown that for the smaller wave-lengths gradient effects significantly increase the value of the true stress at bifurcation. This is not illustrated in Fig. 5, as the stress σ_n shown is an average nominal stress, but the large increases of ϵ_{av} at the onset of localization do reflect the increases of the true stress.

The effect of the magnitude of the initial geometric imperfection δ_0/a_0 is illustrated in Fig. 6, with reference to the curves in Fig. 2. A 10 times smaller imperfection does delay localization a little, both for the

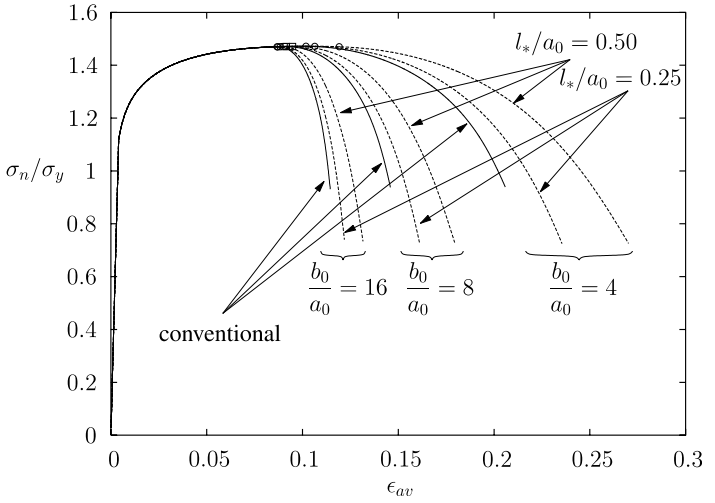

Fig. 4. Overall response in tension for specimens of different aspect ratio ($b_0/a_0 = 4$, 8, and 16). The imperfection is given by $\delta_0/a_0 = 5.0 \times 10^{-3}$, and the material parameters are $\sigma_y/E = 0.004$, $\nu = 0.3$, and $n = 10$. The solid curves show results for a conventional material and the dashed curves show results for a gradient dependent material with $l_*/a_0 = 0.25$ and 0.50.

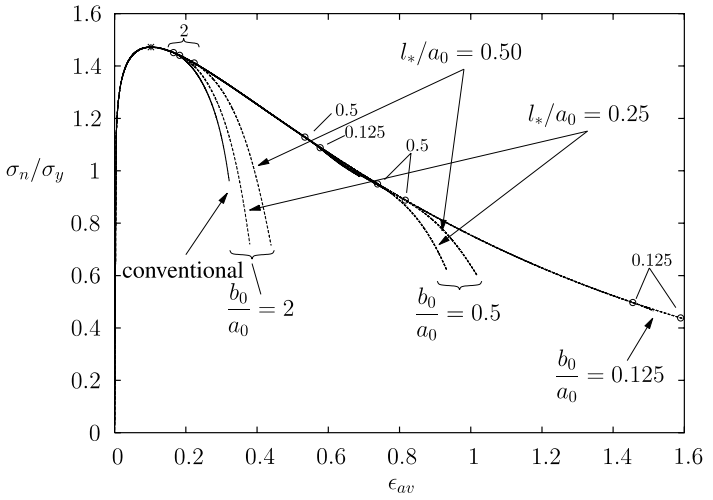

Fig. 5. Overall response in tension for specimens of different aspect ratio ($b_0/a_0 = 1/8$, 1/2, and 2). The imperfection is given by $\delta_0/a_0 = 5.0 \times 10^{-3}$, and the material parameters are $\sigma_y/E = 0.004$, $\nu = 0.3$, and $n = 10$. The solid curves show results for a conventional material and the dashed curves show results for a gradient dependent material with $l_*/a_0 = 0.25$ and 0.50.

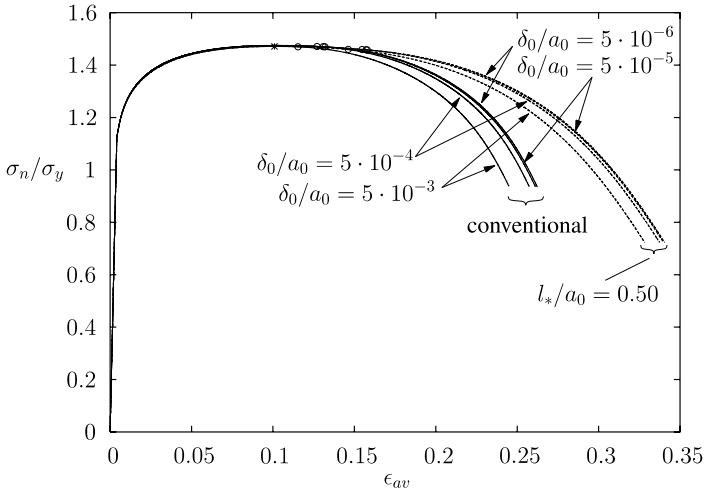

Fig. 6. Overall response in tension for specimens with different initial imperfections. The initial aspect ratio of the specimens is $b_0/a_0 = 3$, and the material parameters are $\sigma_y/E = 0.004$, $\nu = 0.3$, and $n = 10$. The solid curves show results for a conventional material and the dashed curves show results for a gradient dependent material with $l_*/a_0 = 0.50$.

conventional solid and the gradient dependent solid, but rather little additional difference is found for 10^2 or 10^3 times smaller imperfections, indicating that here the curves have converged towards the post-bifurcation behavior of the perfect solid.

The development of the neck as a function of overall strain is shown in Fig. 7 for the same initial imperfection amplitudes as in Fig. 6. It is seen that the small imperfections give almost identical results, which implies that they essentially show the post-bifurcation behavior of a perfect specimen. The solid curves in the figure show results for conventional materials, while the dashed curves show results for gradient

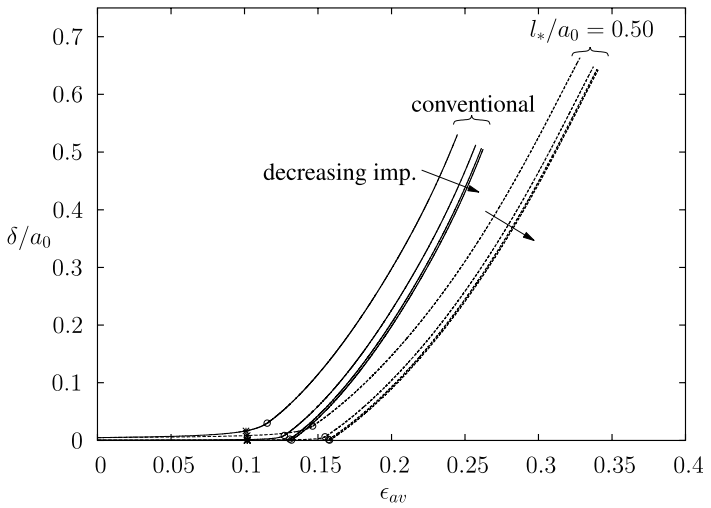

Fig. 7. Neck development in tension for specimens with different initial imperfections. The initial aspect ratio of the specimens is $b_0/a_0 = 3$, and the material parameters are $\sigma_y/E = 0.004$, $\nu = 0.3$, and $n = 10$. The solid curves show results for a conventional material and the dashed curves show results for a gradient dependent material with $l_*/a_0 = 1.00$. The two arrows show how the development of the neck changes when the initial imperfection decreases from $\delta_0/a_0 = 5 \times 10^{-3}$ down to $\delta_0/a_0 = 5 \times 10^{-6}$ changing in factors of 10.

dependent materials with $l_*/a_0 = 0.5$. It is seen that strain gradient hardening has the effect of limiting strain localization and neck development for a given overall strain, when compared to conventional predictions.

4.2. Compression

In Fig. 8 a short, stubby plane strain specimen, $b_0/a_0 = 4$, is analyzed for compressive loading, so that it acts as a stubby column. The initial imperfections considered are in the anti-symmetric mode, as illustrated

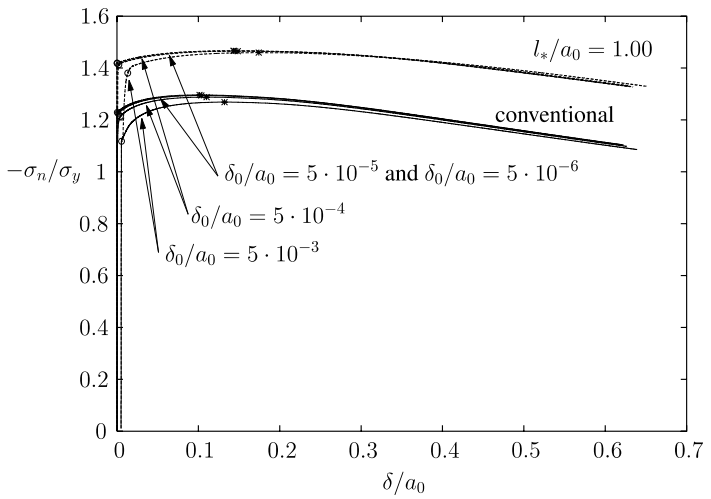

Fig. 8. Overall response in compression for specimens with different initial imperfections. The initial aspect ratio of the specimens is $b_0/a_0 = 4$, and the material parameters are $\sigma_y/E = 0.004$, $\nu = 0.3$, and $n = 10$. The solid curves show results for a conventional material and the dashed curves show results for a gradient dependent material with $l_*/a_0 = 1.00$.

in Fig. 1b, and the diagram shows the average nominal compressive stress $-\sigma_n$ vs. the buckling mode amplitude δ. In Fig. 8 the two smallest imperfections analyzed are small enough to closely follow the bifurcation and post-bifurcation behavior (Hutchinson, 1973). It is characteristic that plastic buckling occurs under increasing load and that a load maximum higher than the bifurcation load is reached on the post-bifurcation path. When the imperfection amplitude is larger, the curves show the characteristic buckling behavior that the load maximum is reduced and that the maximum occurs at a larger value of the mode amplitude (Needleman and Tvergaard, 1980). The curves for the single parameter gradient theory with $l_*/a_0 = 1.0$ show that the buckling load is significantly increased by the gradient effects, as compared with the predictions for the conventional solid.

The choice of the internal higher order boundary condition would have a small but noticeable influence on the results presented Fig. 8, whereas the influence is negligible in the other figures shown until now. For the gradient dependent solid the buckling load as well as the maximum load point are virtually unaffected by the specific choice of higher order boundary condition, but the strain level at the end of the analyses would be increased by a few percent if the full constraint on the plastic strain increment was used instead of the constraint on the higher order traction rate (see the fourth paragraph of Section 4).

In Fig. 9, for a small initial imperfection ($\delta_0/a_0 = 5 \times 10^{-5}$), results of the multi-parameter theory are also shown, with each of the three length parameters set equal to a_0, while the other two are zero. There is rather little difference between the four curves representing strain gradient plasticity, while they all show higher buckling strength than the conventional solid, as in Fig. 8.

Three different values of the initial specimen aspect ratio are considered in Fig. 10. For $b_0/a_0 = 4$ an additional curve is included, $l_*/a_0 = 0.5$, besides the curves already shown in Fig. 8 and 9. For the larger aspect ratio, $b_0/a_0 = 8$, the behavior is affected by the abrupt jump in the tangent modulus at the onset of plastic yielding. Thus, for a perfect column the instability occurs immediately when yielding initiates, and for the small initial imperfection considered in Fig. 10 buckling develops rapidly when a small part of the column material has entered the plastic range.

For the smaller initial aspect ratio, $b_0/a_0 = 2$, no bifurcation is found at all when $l_*/a_0 = 1.0$, even at values of $-\sigma_n/\sigma_y$ far above those shown in Fig. 10. Also, the post-bifurcation behavior for the conventional

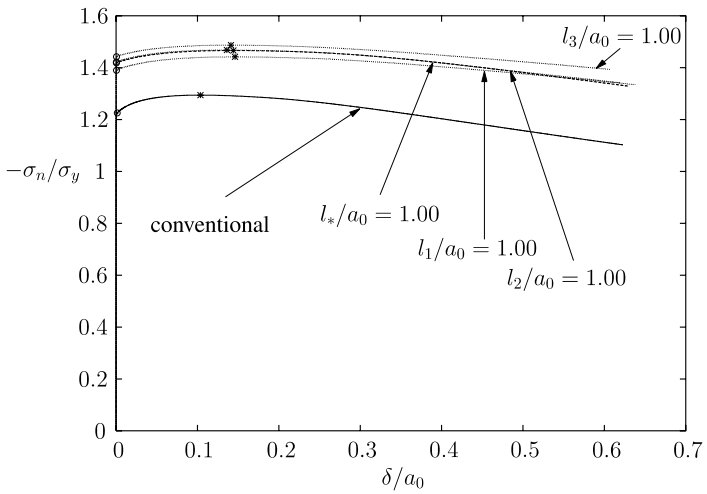

Fig. 9. Overall response in compression for specimens characterized by the geometrical parameters $b_0/a_0 = 4.0$ and $\delta_0/a_0 = 5.0 \times 10^{-5}$, and the material parameters $\sigma_y/E = 0.004$, $\nu = 0.3$, and $n = 10$. The solid curve shows results for a conventional material, while the dashed curve shows results for materials with $l_* = a_0$. The three dotted curves show the results for the multi-parameter theory with each of the material length parameter set equal to a_0 one by one keeping the others zero.

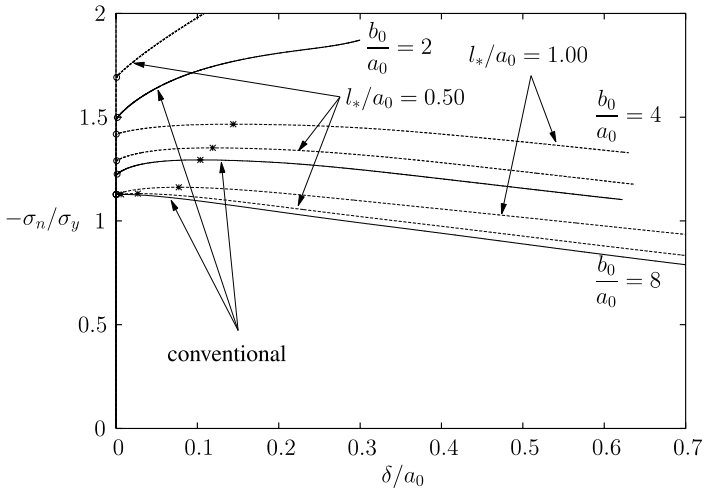

Fig. 10. Overall response in compression for specimens of different aspect ratio ($b_0/a_0 = 2$, 4, and 8). The imperfection is given by $\delta_0/a_0 = 5.0 \times 10^{-5}$, and the material parameters are $\sigma_y/E = 0.004$, $\nu = 0.3$, and $n = 10$. The solid curves show results for a conventional material and the dashed curves show results for a gradient dependent material with $l_*/a_0 = 0.50$ and 1.00.

solid and for $l_*/a_0 = 0.5$ are untypical of buckling, in that no load maximum is found after bifurcation. Here, the current aspect ratio b/a of the specimen at bifurcation is 1.87 for the conventional solid and 1.73 for $l_*/a_0 = 0.5$. It is seen that the current aspect ratio at bifurcation decays rapidly for increasing values of l_*/a_0, so that the first critical bifurcation moves further and further into the short wave range. In this range it is known from Benallal and Tvergaard (1995) that the value of the critical bifurcation stress is highly sensitive to a reduction of the wave-length or an increase of the critical material length, and this explains why no bifurcation is found for $l_*/a_0 = 1.0$ in the range considered.

5. Concluding remarks

Relative to the study of plane strain sheet-necking by Niordson and Redanz (2004) the only improvement of the numerical procedure here lies in the use of higher order elements. The procedure based on triangular elements worked very well for a linear hardening material, but did not show satisfactory converge for a power hardening material, even in the absence of a material length. This surprising problem, which is introduced due to the two-field finite element interpolation, is removed by using the higher order elements, and the results presented in the present paper for a power hardening material have shown excellent convergence.

Both tensile and compressive loading on a plane strain specimen have been analyzed here. For the tensile loading, where bifurcation results in necking, the results show much analogy to those found by Niordson and Redanz (2004), with the difference that the present results are based on a power law representation of the uniaxial tensile test, which can often be used to obtain a good representation of experimental observations. For the plane strain tension–compression test the effect of a gradient plasticity model on the occurrence of bifurcation has been analyzed by Benallal and Tvergaard (1995), and the numerical results obtained in the present paper are related to these bifurcation results, even though the strain gradient plasticity theories used here differ from that in the bifurcation study. Small initial geometrical imperfections are assumed in all the present numerical studies, so that bifurcations do not occur, and the onset of localization or buckling develops gradually from the initial imperfections. However, in several of the studies the

imperfections are so small that the numerical solutions initially follow closely along the pre-bifurcation path, before the bifurcation point is approached, and subsequently the post-bifurcation path is closely followed, so that in fact these computations give a very good representation of the bifurcation and post-bifurcation behavior of the specimens.

For larger values of the initial aspect ratio of the specimen, both tensile and compressive tests follow standard behavior. In tension, the onset of necking is delayed beyond the load maximum due to the finite aspect ratio, and is further delayed by the effect of gradient hardening. In compression, a load maximum is reached after bifurcation, on the post-bifurcation path, and as usual the buckling load is higher the shorter the column, but the buckling load is further increased by the effect of gradient hardening.

For small values of b_0/a_0 the bifurcation mode wave-length is forced to be small relative to the specimen width, and it is known from the earlier bifurcation results that this significantly delays the onset of bifurcation in the presence of gradient hardening. Here tension or compression give a different trend, as illustrated in Figs. 5 and 10. In tension, for $b_0/a_0 = 0.125$ and gradient hardening with $l_*/a_0 = 0.5$, the onset of localization is delayed to such a large strain that the current aspect ratio of the deformed specimen is increased by a factor 20, which changes the behavior of the specimen to one with a much higher aspect ratio but with a relatively stronger gradient effect. By contrast, in compression with $b_0/a_0 = 2$ the current aspect ratio grows smaller as the load is increased, so that the specimen is deformed into a range where the delay due to the gradient effect keeps increasing, and this is the reason why no bifurcation was found for the value of l_*/a_0 as large as 1. A common feature of tension and compression is that with gradient hardening present we have not found instabilities corresponding to very short wave modes, approaching the so-called surface wave instabilities.

Acknowledgment

This work is financially supported by the Danish Technical Research Council in a project entitled Modeling Plasticity at the Micron Scale.

References

Aifantis, E.C., 1984. On the microstructural origin of certain inelastic models. Transactions of the ASME. Journal of Engineering Materials and Technology 106 (4), 326–330.

Begley, M.R., Hutchinson, J.W., 1998. Mechanics of size-dependent indentation. Journal of the Mechanics and Physics of Solids 46 (10), 2049–2068.

Benallal, A., Tvergaard, V., 1995. Nonlocal continuum effects on bifurcation in the plane strain tension–compression test. Journal of the Mechanics and Physics of Solids 43 (5), 741–770.

de Borst, R., Mühlhaus, H.-B., 1992. Gradient-dependent plasticity: formulation and algorithmic aspects. International Journal for Numerical Methods in Engineering 35, 521–539.

de Borst, R., Pamin, J., 1996. Some novel developments in finite element procedures for gradient-dependent plasticity. International Journal for Numerical Methods in Engineering 39, 2477–2505.

Fleck, N.A., Hutchinson, J.W., 1997. Strain gradient plasticity. In: Hutchinson, J.W., Wu, T.Y. (Eds.), Advances in Applied Mechanics, vol. 33, Academic Press, New York, pp. 295–361.

Fleck, N.A., Hutchinson, J.W., 2001. A reformulation of strain gradient plasticity. Journal of the Mechanics and Physics of Solids 49, 2245–2271.

Fleck, N.A., Muller, G.M., Ashby, M.F., Hutchinson, J.W., 1994. Strain gradient plasticity: theory and experiment. Acta Metallurgica et Materialia 42 (2), 475–487.

Haque, M.A., Saif, M.T.A., 2003. Strain gradient effect in nanoscale thin films. Acta Materialia 51 (11), 3053–3061.

Hill, R., Hutchinson, J.W., 1975. Bifurcation phenomena in the plane tension test. Journal of the Mechanics and Physics of Solids 23, 239–264.

Hutchinson, J.W., 1973. Post-bifurcation behavior in the plastic range. Journal of the Mechanics and Physics of Solids 21, 163–190.

Ma, Q., Clarke, D.R., 1995. Size dependent hardness of silver single crystals. Journal of Materials Research 10, 853–863.
McMeeking, R.M., Rice, J.R., 1975. Finite-element formulations for problems of large elastic–plastic deformation. International Journal of Solids and Structures 11, 601–616.
Mühlhaus, Aifantis, E.C., 1991. A variational principle for gradient plasticity. International Journal of Solids and Structures 28 (7), 845–857.
Needleman, A., Tvergaard, V., 1980. Aspects of plastic post-buckling behaviourMechanics of Solids, The Rodney Hill 60th Anniversary Volume. Pergamon Press, Oxford, pp. 453–498.
Niordson, C.F., Hutchinson, J.W., 2003. Non-uniform plastic deformation of micron scale objects. International Journal for Numerical Methods in Engineering 56, 961–975.
Niordson, C.F., Redanz, P., 2004. Size-effects in plane strain sheet-necking. Journal of the Mechanics and Physics of Solids 52, 2431–2454.
Stölken, J.S., Evans, A., 1998. A microbend test method for measuring the plasticity length scale. Acta Materialia 46 (14), 5109–5115.
Vardoulakis, I., Aifantis, E., 1991. A gradient flow theory of plasticity for granular materials. Acta Mechanica 87, 197–217.
Yamada, Y., Sasaki, M., 1995. Elastic–plastic large deformation analysis program and lamina compression test. International Journal of Mechanical Sciences 37, 691–707.
Young, N., 1976. Bifurcation phenomena in the plane compression test. Journal of the Mechanics and Physics of Solids 24, 77–91.
Zienkiewicz, O., 1977. The Finite Element Method, third ed. McGraw-Hill, London.